Journal of Microscopy, Vol. 178, Pt 3, June 1995, pp. 251–260.
Received 21 February 1994; accepted 30 January 1995

Analysis of the spatial distribution of AgNOR proteins in cell nuclei using simultaneous confocal scanning laser fluorescence and transmitted light microscopy

F. PARAZZA,* E. BERTIN,* Z. WOZNIAK† & Y. USSON*
**DyOGen & TIMC-IMAG, Institut Albert Bonniot, Université Joseph Fourier, La Tronche, France*
†Equipe de Cytologie Quantitative, Faculté de Médicine, Grenoble, France and Department of Pathology, Academy of Medicine, Woclow, Poland

Key words. Confocal scanning laser microscopy, three-dimensional imaging, three-dimensional image analysis, nucleolus, AgNOR, leukaemia.

Summary

The selective staining of nucleolar acidic proteins by silver dyes (AgNOR technique) is a promising tool to discriminate malignant cells from benign cells in tumour pathology. Until now, the existing methods to measure the distribution of the AgNOR proteins were performed in two-dimensional space. Confocal scanning laser microscopy (CSLM) and progress in computer sciences make it possible to image biological specimens in three dimensions. We have used these techniques to develop a method to discriminate cells by comparing the three-dimensional (3-D) spatial distribution of the AgNOR proteins. The distribution of the AgNOR proteins was described by the following measurements: the volume fraction of the nucleus occupied by the AgNOR-stained aggregates, the distances between the aggregates, their number per nucleus, the distance of each aggregate from the nuclear border and their anisotropy. CSLM was used to acquire simultaneously the 3-D data set of the nucleus (confocal fluorescence) and the 3-D data set of the location of the AgNOR proteins (brightfield transmission). Two biases, due to the different modes of microscopy and the silver labelling technique, had to be taken into account in the evaluation of the measurements. A preliminary study on three lines of lymphocytic cells shows that these parameters are discriminatory. Thus, this method makes it possible to combine two different modes of scanning laser microscopy for a 3-D quantitative analysis and is potentially useful for assessing the spatial distribution of AgNOR proteins in tumour pathology.

Introduction

The nucleolar organizer regions (NORs) are the genomic DNA segments encoding for ribosomal RNA (rRNA). In human somatic cells, NORs appear on the short arms of the five acrocentric chromosomes (numbers 13, 14, 15, 21 and 22; Howell, 1982). During interphase, the NORs are located in the fibrillar components of nucleoli (Wachtler *et al.*, 1986). They can be visualized in chromosome preparations and in interphase nuclei because NORs are associated with argyrophilic proteins (AgNOR technique) involved in the regulation of transcription or post-transcriptional modification of rRNA transcripts. The silver-staining technique for the demonstration of the NORs was originally used to demonstrate NORs in cytogenetic preparations (Howell & Black, 1980). The technique was simplified and first applied to histological and cytological preparations by Ploton *et al.* (1982). In recent years it has been demonstrated that the quantity of interphase AgNOR proteins is related to the cell proliferation rate. This observation indicates that the quantification of interphase AgNOR proteins may be useful for the evaluation of cell kinetics. It was demonstrated that the distribution of interphase AgNOR proteins can be used to distinguish malignant cells from corresponding benign or normal cells on the basis of higher quantity of interphase AgNOR proteins. Moreover, it has been suggested that the AgNOR staining will give new, diagnostic and prognostic information in tumour pathology (Ploton *et al.*, 1986).

Initially, silver-stained interphase NORs were counted as usual (Crocker & Skilbeck, 1987) using brightfield microscopy. Many subsequent studies of the distribution of interphase NORs have been made in different tumour tissues (for review see Derenzini & Ploton, 1991; Egan & Crocker, 1992). In many of these analyses, the distribution of the NORs was characterized by the number of NORs in each nucleus. In some of these studies, the mean nuclear area fraction occupied by the silver-stained NORs was added to the previous parameter (Derenzini *et al.*, 1989). Today, quantitative measurements of the NORs can be

Correspondence: Yves Usson, DyOGen, Institute Albert Bonniot, Université Joseph Fourier, 38706 La Tronche cedex, France. Yves.Usson@ujf-grenoble.fr

made with dedicated software running on image cytometers (Rüschoff *et al.*, 1990; Guillaud *et al.*, 1993). All these studies use a two-dimensional (2-D) representation (planar image of the brightfield microscope) of the 3-D distribution of NORs. The loss of the third dimension introduces a bias in the analysis of the distribution of the NORs. Furthermore, the weak axial resolution of the conventional brightfield microscope increases the difficulty of segmenting the AgNOR aggregates. Progress in microscopy and in computer sciences makes it possible to obtain 3-D data. Descriptions of the architecture of nucleoli and topographical distribution of NORs have been made in three dimensions using confocal scanning laser microscopy (CSLM) (Hernandez-Verdun *et al.*, 1991; Beorchia *et al.*, 1993; Robert-Fortel *et al.*, 1993).

However, the previous studies were qualitative and hence neither quantitative nor statistical data are available for the analysis of the spatial distribution of NORs in cell nuclei. Today, computer science provides powerful and efficient tools for the analysis of 3-D microscopic data (Preston & Siderits, 1992; Carter *et al.*, 1993). In this paper, we propose a quantitative method to discriminate cells belonging to different cell lines by the characterization of the 3-D distribution of NORs in cell nuclei using both fluorescence CSLM and laser scanning brightfield microscopy.

Material and methods

Specimens

Cell lines (kindly provided by Dr Pierre Champelovier) HL60 (Gallagher *et al.*, 1979), K562 (Lozzio & Lozzio, 1975) and LAMA 84 (Seigneurin *et al.*, 1987) derived from leukaemic patients were cultured in suspension culture (RPMI 1640, Boehringer) supplemented with 10% fetal calf serum (FCS-Gibco) 100 IU/ml, Penicillin and 100 mg/ml streptomycin in humidified atmosphere (5% CO_2, 95% air) at 310 K. The medium was changed twice weekly.

Cell lines were fixed and stained with silver as described by Ploton *et al.* (1982). Briefly, 2 ml of suspension culture containing 10^6 cells was centrifuged for 5 min at 800 rpm and resuspended in 4% paraformaldehyde for 10 min. Approximately 50 000 cells were applied per slide and centrifuged at 700 rpm for 5 min using a Cytospin (Shandon). The preparations were washed for 10 min in deionized water. The slides were then covered with a freshly made up staining solution prepared by mixing equal volumes of two solutions: (i) 0·5 ml/ml of $AgNO_3$ (Merck) in deionized water; (ii) 1 mg/ml of gelatine in 2% (by vol.) formic acid. The slides were incubated for 25 min at room temperature. After staining, they were washed in bidistilled water, rinsed in 5% thiosulphate solution for 10 min, then rinsed in water. For defining the boundaries of nuclei, DNA was stained with propidium iodide/RNase cocktail. Slides were then washed three times in distilled water and mounted in 30 μl of antifade solution (2·3% w/v DABCO in 90% glycerol 0·1 M Tris, pH 7·5). The medium refractive index (1·51) is close enough to the oil index (1·518) to prevent a bias along the axial direction (optical axis) during the acquisition step.

Data acquisition

The optical sections through the AgNOR proteins and the nucleus were sampled simultaneously using an LSM 410 confocal scanning laser inverted microscope (Carl Zeiss, Oberkochen, Germany) fitted with a 63×, NA 1·4, Plan-Apochromat oil-immersion objective. The AgNOR proteins were imaged in laser scanning brightfield transmitted light mode while the nucleus (propidium-iodide-stained) was imaged in confocal scanning laser fluorescence mode. In fluorescence mode (nucleus imaging), a 514-nm band laser beam was used for the excitation of the propidium iodide and the emitted fluorescence was filtered by a 560-nm beamsplitter followed by a 590-nm long-pass filter. For the transmission mode (AgNOR proteins imaging), the same laser beam was used to avoid differences in focal planes. The voxels were sampled every 0·12 μm in the focal plane and the microscope stage was raised 0·24 μm between the recording of each optical section. The quantification of signal intensity was done on an 8-bit scale (256 grey-level values). Each optical section was recorded with a scanning time of 0·5 s per field. This scanning time was long enough to obtain a good signal-to-noise ratio while limiting the fading of the propidium iodide (PI) fluorescence. For each sample, the optical sections were stored as two series of 60 digital images (128 × 128 pixels) corresponding to two final volumes of 15·36 μm by 15·36 μm by 14·40 μm. The volume acquired by fluorescence CLSM corresponded to the confocal optical sections of the nucleus (NU volume) and the other one corresponded to the optical sections of the AgNOR proteins (AG volume).

Computer equipment

The digital volumes were transferred and stored on a workstation via a high-speed IEEE-488 communication line. Since the amount of data was huge, they were archived on a digital audio tape device (1·2 Gbyte per tape). Analysis of the digital volumes was performed on an Iris Indigo Entry workstation (Silicon Graphics, Mountain View, U.S.A.). This UNIX workstation was fitted with an RS 4000 RISC processor and 64 Mbytes RAM. The analysis software and 3-D visualization software were written in standard C language using the GL library (Silicon Graphics library) and the FORMS user interface library (courtesy of Mark Overmars, Department of Computer Science, Utrecht University, the Netherlands).

Image analysis

We have developed a program to extract measurements from the 3-D data sets. The features were: (i) morphological parameters such as the number of AgNOR-stained aggregates, their averaged volume fraction and the associated standard deviation; (ii) quantities related to the spatial distribution of the aggregates, such as the normalized average distance of the AgNOR-stained aggregates from the nuclear border, the normalized average distance to the nearest neighbour of each aggregate, and their respective standard deviations; (iii) the anisotropy properties as given by the latent roots of the matrix of direction cosines.

Processing of the AgNOR data set. A 3-D median operator (a cubic kernel of $3 \times 3 \times 3$ voxels without the corner voxels) was first used to eliminate the pulse noise from the digital volume (van der Voort *et al.*, 1989). Because the *AG* data were collected in non-confocal mode, the axial resolution achieved was much lower than that of the *NU* data. In order to compensate for the difference in resolution, a restoration process was performed on the *AG* data sets. This restoration filter (Parazza *et al.*, 1993) is based on a simplified implementation of the nearest–neighbour method (Castleman, 1979).

After this pre-processing step, the AgNOR-stained aggregates were segmented by grey-level thresholding. The value of the threshold was interactively set using three orthogonal 'cross-section' views (*xy*, *yz* and *xz*) of the digital volume. Thus, the user could visually assess the effect of the chosen threshold value on the entire *AG* volume.

Then, the connected components corresponding to each AgNOR-stained aggregate were labelled using a seed-fill algorithm (Parazza *et al.*, 1993). After this labelling step, the volume of each aggregate was calculated by counting the number of voxels with the same label.

In order to compute distances between aggregates, distances from the border of the nucleus and other parameters, the gravity centre of each labelled aggregate was extracted. The coordinates (g_x, g_y, g_z) of the *j*th aggregate gravity centre GA_j were computed as follows:

$$g_x = \frac{x_{\text{res}}}{n} \times \sum_{i=1}^{n} p_{x_i} \quad g_y = \frac{y_{\text{res}}}{n} \times \sum_{i=1}^{n} p_{y_i} \quad g_z = \frac{z_{\text{res}}}{n} \times \sum_{i=1}^{n} p_{z_i}$$

where p_{x_i}, p_{y_i}, p_{z_i} are the indices of the *i*th voxel of the *j*th object, n is the number of voxels of the *j*th object and x_{res}, y_{res}, z_{res} are the sampling steps in the three directions.

Processing of the nucleus data set. The pulse noise was filtered out from the *NU* data sets using the same median filter as for the *AG* data sets. Since the data were collected in confocal mode, there was no need for a blur removal filtering. A grey-level thresholding was used to segment the *NU* volume and a 3-D interactive extraction (based on the seed fill algorithm) was used to find the nuclear voxels.

A bias due to the high opacity of the silver staining was clearly seen at this step of the process: the AgNOR-stained aggregates created a shadowing effect beneath their locations in the nucleus sections. The fluorochromes located under the aggregates were not uniformly excited and the light they emitted was partially blocked. This effect resulted in conical shadows under the locations of the AgNOR-stained aggregates in the nucleus sections (Fig. 1). In some cases, after segmentation, aggregates could, surprisingly, be seen outside the nucleus. Consequently, the presumed boundaries of the nucleus had to be retrieved before the distance calculations. We chose to approximate the boundaries of the nucleus by its convex hull. The convex hull of a nucleus is the smallest convex polyhedron that contains its boundary voxels.

The method we developed to extract the convex hull is based on the Voronoï diagram. In a first step, the voxels *Vs* belonging to the surface of the nucleus were extracted. This extraction was done by checking the neighbourhood of each voxel belonging to the nucleus: if at least one of its 26 neighbours was not a nucleus voxel (background voxel), the current voxel belonged to the surface of the nucleus. Each voxel *Vs* was considered as a seed p_i with coordinates expressed in real distances. The location of each seed must be expressed in real coordinates since the computation of the Voronoï tessellation requires an isotropic metric. The seeds were stored in the set of the surface seeds *SP* and the Voronoï

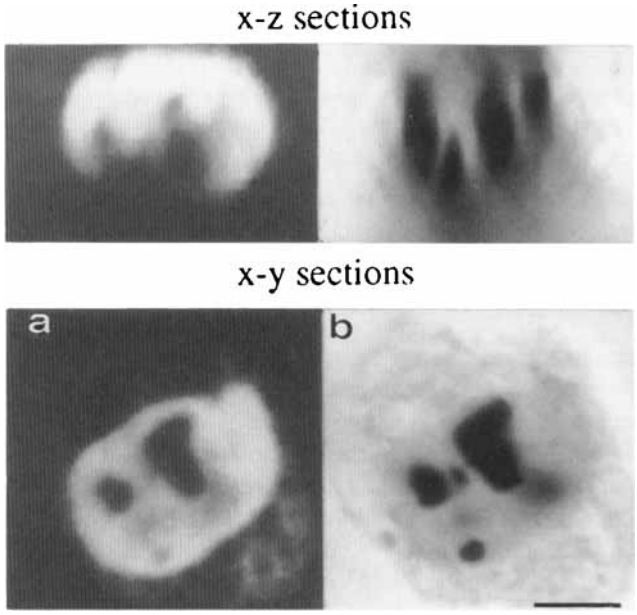

Fig. 1. Axial (*xz*) and in-focus (*xy*) fluorescence of the nucleus (left) and images of the AgNOR-stained aggregates (right). The shadowing effect of the silver-stained aggregates produces discontinuities in the shape of the nucleus.

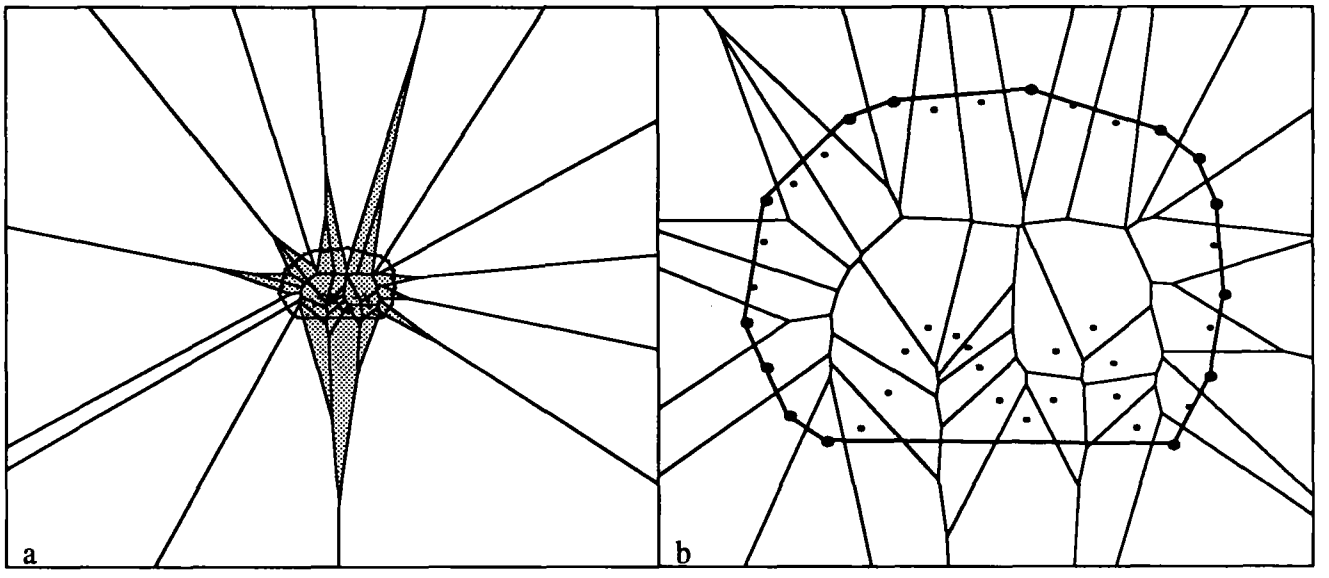

Fig. 2. These two images represent the 2-D Voronoï construction on a simulated set of surface points (*xz* border of nucleus). The bounded polygons (a) are shaded and the unbounded polygons are in white. A magnified view of the same Voronoï diagram (b) shows the details of the polygonal representation of the convex hull. The black points associated with unbounded polygons belong to the convex hull. The grey points are associated with bounded polygons and consequently do not belong to the convex hull.

diagram was built on this set. The Voronoï diagram *VD* is a partition of the space into Voronoï polyhedra. For each seed P_i belonging to *SP*, the Voronoï polyhedron $Vor(p_i)$ associated to p_i is the region of the space where every point in $Vor(p_i)$ is closer to P_i than to any other point p of *SP*:

$$Vor(p_i) = \{x \in R^3,\ d(x,p_i) \leqslant d(x,p),\ \forall p \in SP - p_i\}$$

where d is the Euclidean distance. $Vor(p_i)$ is polyhedral and convex.

The computation of the Voronoï diagram (Bertin *et al.*, 1993) is based on an improvement of the incremental Boywer's algorithm (Boywer, 1983). In practice, this diagrammatic construction needs an initialization step to define the notion of unbounded space: four 'imaginary seeds' are set at the vertex of a large tetrahedron surrounding the volume of the nucleus. The size of this tetrahedron is very large (×10 000) compared to the amplitude of the point coordinates in the set *SP*. All the seeds p added to the Voronoï diagram during the incrementation step are included in this tetrahedron volume.

The convex hull seeds can be extracted from the Voronoï diagram since a property of this tessellation (Preparata & Shamos, 1985) assumes that a seed p_i of *SP* belongs to the convex hull *CH* of the set of points *SP* if and only if its associated polygons $Vor(p_i)$ are unbounded (Fig. 2). If this property was used in the convex hull extraction process, we would have obtained the set of the nucleus surface seeds belonging to the convex hull instead of having the surface representation of the convex hull (triangulation surface). In order to obtain the triangulation of the convex hull, a property of the dual diagram of the Voronoï diagram (Delaunay tetrahedrization) was used in addition to the previous one: the Delaunay tetrahedrization of the set *SP* is a partition of the convex hull of the set *SP* (if the imaginary seeds are not considered). Therefore, a triangle (made by three seeds of *SP*) belongs to the convex hull triangulation if and only if one of these two associated Delaunay tetrahedra contains a unique imaginary seed. Practically, the four generator seeds (Delaunay tetrahedron) of each vertex of each Voronoï polyhedron were checked: if one and only one of these seeds was an imaginary seed, then the three others formed a triangle of the convex hull triangulation.

Measurements. The estimation of the parameters was based on the general model assumption of a stationary hard-core point process model (König *et al.*, 1989, 1991). In order to avoid bias induced by the different sizes of nuclei on these measurements, all the distances were normalized by a reference distance. This distance *Dnorm* was the shortest distance between the nuclear gravity centre and the border of the nucleus from which the radius of the smallest particle size (AgNOR aggregate) in the nucleus was subtracted. The gravity centre of the nucleus *GN* was computed using the seeds if *SP*. *Dnorm* was calculated by comparing the distances between *GN* and each plane *P* (defined by the three vertices of each triangle of *CH*). These distances were computed using an orthogonal projection of *GN* on *P* (see Appendix). The shortest distance of each aggregate from the nuclear border was found using the method described above (orthogonal projection). This distance was normalized by

the distance *Dnorm*. The mean of these distances and the standard deviation were computed for each nucleus. The mean and standard deviation were computed for: (i) the distance between each pair of aggregates; (ii) the distance of each aggregate to its closest neighbour.

The morphological parameters were the number of AgNOR aggregates (found in the labelling step of the *AG* data set), the average volume fraction of AgNOR aggregates and the associated standard deviation. The volume fraction was calculated by dividing the volume of an aggregate by the volume of the convex hull of the nucleus (sum of the volumes of each tetrahedron formed by the three seeds of a convex hull triangle and the gravity centre).

In order to measure the anisotropy of the distribution of AgNOR-stained aggregates in the nucleus, we define 3-D unitary vectors along the direction of the gravity centre of the nucleus *GN* to each gravity centre of AgNOR-stained aggregates *GA*. The estimate of anisotropy of the spatial distribution of the aggregates was given by the values of the latent roots of the matrix of direction cosines of these vectors. This method was introduced by Anderson & Stephens (1972) and was applied by other authors for the characterization of fibre processes in the context of confocal microscopy (Mattfeldt *et al.*, 1994; Usson *et al.*, 1994). In samples from perfectly isotropic aggregates the eigenvalues will be $\approx 1/3$.

Results

In order to evaluate the discriminating power of the measurements, three lines of lymphocytic cells were analysed (HL60, K562 and LAMA84). The acquisition of about 33 cells per line was made using the confocal scanning laser microscope. For each nucleus, the restoration and the extraction of the different parameters was made as described above. For the three lines the mean and standard deviation of each parameter are shown in Table 1. Three kinds of parameters were calculated per nucleus: (i) morphological ones such as the mean number of aggregates per nucleus (*NbNOR*), the volume of the nuclear convex hull (*VCH*), the average volume fraction of the aggregates (*AV*) and the standard deviation of the average volume fraction between nuclei (*SV*); (ii) topographical ones such as the normalized average distance of the AgNOR aggregates from the nuclear border (*ADE*), the standard deviation of the normalized distance of the AgNOR aggregates from the nuclear border (*SDE*), the normalized average distance of an aggregate to its nearest neighbour (*AN*) and the standard deviation of this distance (*SN*); (iii) anisotropy properties, such as the two normalized eigenvalues (*EV1* and *EV2*). It appeared that, when considered separately, the variables made it possible to distinguish HL60 nuclei from those of the two other cell lines. In HL60, the values of *NbNOR*, *AV*, *SV*, *ADE* and *AN* were significantly different from those obtained in LAMA84 and K562 cells. In particular, the number of AgNORs in HL60 was very small ($5{\cdot}47 \pm 2{\cdot}0$). Also, the values of *SDE* and *SN* were significantly smaller in LAMA84 nuclei. No significant differences were observed for the nuclear volume (*VCH*) and the eigenvalues *EV1* and *EV2*. Here, the values of *EV1* were much greater than 0·3, indicating that the distribution of aggregates was anisotropic. The values suggested that the AgNORs were mainly distributed inside a 3-D ellipsoid. However, in the case of HL60, *EV1* and *EV2* values should be interpreted with care because the number of aggregates is small and very close to the number of dimensions (3) used for the directional statistics. Nevertheless, to overcome this problem the directional statistics were calculated only with nuclei (28 out of 33) whose number of aggregates was greater than 5, i.e. at least twice the number of dimensions.

All the parameters were submitted to a factorial discriminant analysis (FDA). Figure 5 shows the projections of the cell measurements on the two discriminant factorial axes. The factorial axes represent the linear combinations of the parameters which emphasize the differences between populations. Almost all the cells belonging to a cell line are included in the confidence ellipse of the population (95% confidence) (Fig. 5). We see that each population is sufficiently clustered and separated from the others to be recognized unambiguously. This is confirmed by the confusion matrix, which shows a

Table 1. Extracted parameters. The parameters are calculated for each cell. The table shows the mean and standard deviation of these parameters for the cell lines. *NbNOR* is the number of AgNOR aggregates in a nucleus; *VCH* is the volume of the nuclear convex hull (μm^3); *AV* is the average volume fraction of one aggregate; *SV* is the scatter of the average volume fraction; *ADE* is the normalized average distance of the AgNOR aggregates from the nuclear border; *SDE* is the scatter of the normalized distance of the AgNOR aggregates from the nuclear border; *AN* is the normalized average distance of an aggregate to its nearest neighbour; *SN* is the scatter of this average distance; *EV1* and *EV2* are, respectively, the first and the second eigenvalue of the matrix of cosines normalized by the sum of the three eigenvalues.

Cell line	HL60	Lama84	K562
NbNOR	$5{\cdot}47 \pm 2$	$16{\cdot}57 \pm 3{\cdot}08$	$21{\cdot}51 \pm 6{\cdot}02$
VCH	463 ± 114	511 ± 119	529 ± 105
AV	$0{\cdot}30 \pm 0{\cdot}16$	$0{\cdot}06 \pm 0{\cdot}02$	$0{\cdot}07 \pm 0{\cdot}03$
SV	$0{\cdot}25 \pm 0{\cdot}18$	$0{\cdot}04 \pm 0{\cdot}02$	$0{\cdot}12 \pm 0{\cdot}04$
ADE	$17{\cdot}29 \pm 6{\cdot}46$	$5{\cdot}25 \pm 1{\cdot}04$	$8{\cdot}11 \pm 2{\cdot}91$
SDE	$33{\cdot}53 \pm 9{\cdot}27$	$20{\cdot}35 \pm 3{\cdot}11$	$34{\cdot}66 \pm 7{\cdot}9$
AN	$11{\cdot}38 \pm 6{\cdot}76$	$2{\cdot}16 \pm 0{\cdot}83$	$3{\cdot}54 \pm 2{\cdot}15$
SN	$21{\cdot}20 \pm 9{\cdot}89$	$8{\cdot}32 \pm 2{\cdot}29$	$14{\cdot}69 \pm 7{\cdot}34$
EV1	$0{\cdot}57 \pm 0{\cdot}08$	$0{\cdot}49 \pm 0{\cdot}03$	$0{\cdot}50 \pm 0{\cdot}06$
EV2	$0{\cdot}31 \pm 0{\cdot}06$	$0{\cdot}32 \pm 0{\cdot}04$	$0{\cdot}33 \pm 0{\cdot}04$

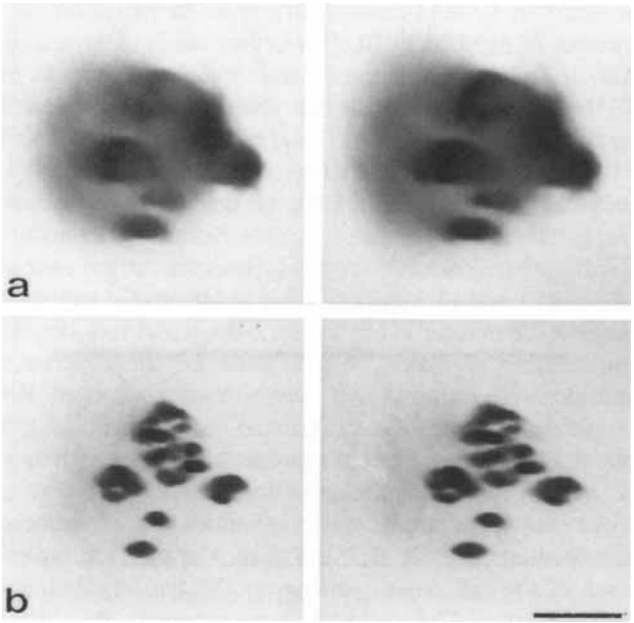

Fig. 3. Effect of the deblurring of the AgNOR-stained aggregates. The two stereo-pairs show a 3-D transparency reconstruction of the same AG data set, before (a) and after (b) the deblurring process. The data have been rotated by 50° around the y-axis. In (a) it is difficult to see distinctly the AgNOR aggregates (out-of-focus haze), whereas in (b) the aggregates are sharp enough to be separated.

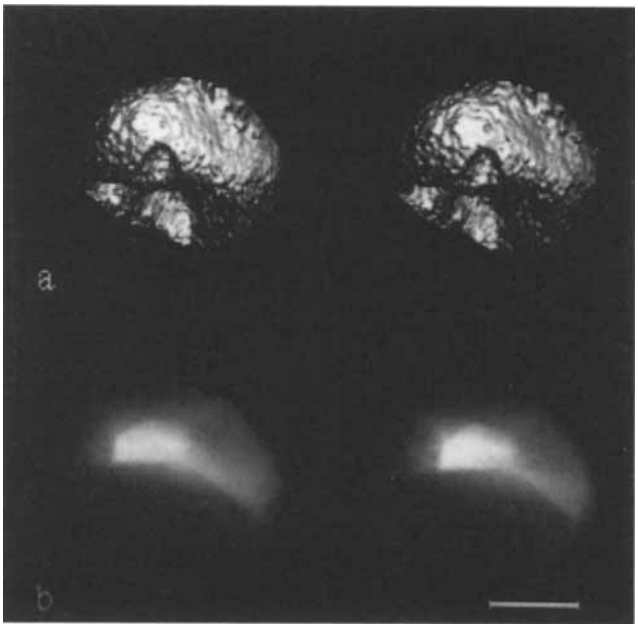

Fig. 4. Effect of the surface restoration of the nucleus. (a) A 3-D surface reconstruction of the border of the nucleus with a viewing angle of 120° around the x-axis. We can see artefactual invaginations caused by the silver staining. (b) The 3-D reconstruction (same viewing point) of the triangulation of the convex hull associated with the nucleus.

percentage of good classification of 99%. In conclusion, the characterization of the different parameters was sufficient to discriminate cells belonging to the three different leukaemic cell lines.

Discussion

The aim of the present work was to find a method to characterize the spatial distribution of AgNOR proteins in cell nuclei in order to differentiate cells belonging to different cell lines. In order to characterize the spatial distribution, we used a series of parameters to quantify the topography, the morphology and the anisotropy. Two major biases had to be considered in order to compute these parameters: the lack of depth resolution in the sections of AgNOR proteins (non-confocal optical sections) and the shadowing effect of the silver staining on the propidium iodide fluorescence of the nucleus. After the restoration procedure the significant voxels have to be found by a segmentation procedure.

Restoration of AgNOR data set

The effect of the image restoration by the modified nearest-neighbour algorithm is shown in Fig. 3. These views were obtained with a home-made 3-D reconstruction package based on a ray-casting model (Robb & Barillot, 1988). Figure 3 makes it possible to assess the improvement of resolution obtained by the deblurring method. Figure 3(a) shows the reconstruction of the raw data. AgNOR aggregates appear as 5 or 6 large fuzzy clumps surrounded by out-of-focus haze. Figure 3(b) shows the reconstruction of the deblurred data. The out-of-focus haze has disappeared and a large number of sharp dots are clearly visible.

It can be seen that the AgNOR aggregates appeared to be slightly elongated along the optical axis. This artefact is due to the limits of the restoration technique. The nearest-neighbour algorithm is one of many methods. These techniques have been described and compared in the literature (Agard *et al.*, 1989; Conchello & Hansen, 1989; for review see Shaw & Rawlins, 1991). They offer different advantages: some are dedicated to fluorescence images while others are more efficient for brightfield transmitted light images (Willis *et al.*, 1993). The nearest-neighbour algorithm offers the least degree of restoration. However, the other methods are time-consuming and consequently can hardly be included in a repetitive process of analysis. The nearest-neighbour deblurring algorithm offers the best quality versus time ratio.

Restoration of nuclear data set

The result of the restoration of the presumed shape of a nucleus by a convex hull triangulation is shown in Fig. 4. The stereo-pairs of the segmentation of the raw nucleus were made with the 3-D reconstruction programme using a surface rendering model (Gordon & Reynolds, 1985). The stereo-pairs of the convex hull were made using the GL rendering library (Silicon Graphics). The nucleus is viewed from the rear at a slight angle. In Fig. 4(a), large cavities can be seen on the base of the nucleus. These result from the shadowing effect of the silver staining. The restoration based on the 3-D convex hull triangulation (Fig. 4b) gives a smooth surface and fills the cavities at the base of the nucleus.

The choice of a time-consuming method to restore the putative shape of the nucleus should be considered since faster approaches have been proposed to approximate the shape of the nucleus by an ellipsoid (Kett *et al.*, 1992; Usson *et al.*, 1994). However, in these studies, only the main orientation of the nucleus was of interest. In the present study, we tried to obtain a more realistic representation of the nucleus: the convex hull triangulation perfectly fits the convex regions of the nuclear surface and fills concave artefactual regions.

The original version of the Voronoï diagram computation was time-consuming since its algorithmic complexity was in $O(n^2\sqrt{n})$ (where n is the number of seeds). The amelioration of Boywer's algorithm led to a Voronoï diagram computational complexity in $O(n\log(n))$. Details of this amelioration can be found in Bertin (1994).

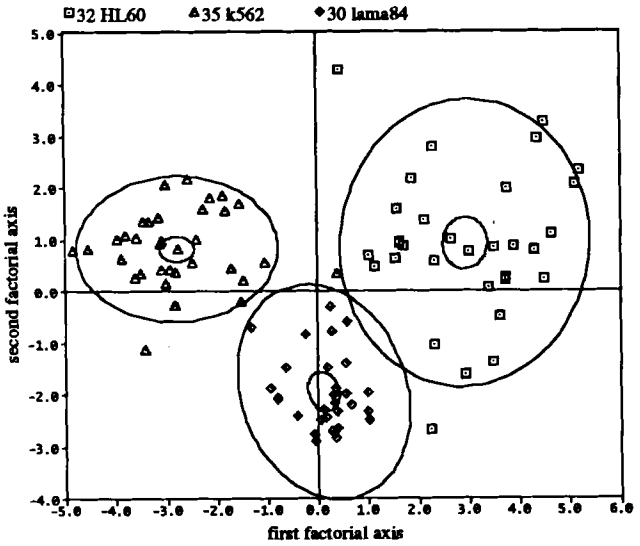

Fig. 5. The factorial discriminant analysis. All the cells belonging to the three cell lines are projected in the space defined by the two factorial discriminant axes. Almost all the cells belonging to the same cell line are included in the confidence ellispe (95% confidence). Each of the three analysed populations is concentrated and separated sufficiently from the others to be distinctly recognized.

Nevertheless, the surface restoration remained the longest process of the method along with the deblurring process. Other algorithms of calculation of the 3-D convex hull have been presented in the literature with equivalent performance or higher if they are considered in their parallel version (Day, 1991; Reif & Son, 1992). However, the graph structure of Voronoï tessellation used gave us a powerful tool for 3-D surface or intravolume measurements (Bertin *et al.*, 1993).

Before computation of the Voronoï diagram, it must be verified that in no case are five seeds of the surface point sets on the same virtual sphere and no four seeds on the same virtual circle. These conditions were necessary to improve the diagram construction and to obtain a triangulation of the convex hull. In our case, because the seeds were extracted from a voxel representation, there was a high probability of finding five cospherical seeds and four cocircular seeds in the set. Therefore, before the Voronoï diagram computation, each seed position has been randomly moved around their actual location. The maximal shift added to each of the coordinates was 1% of the sampling step values. The addition of random noise in the locations of seeds strongly reduced the probability of encountering the two undesirable geometrical configurations. The effect of this process on the volume and distance measurements has been checked on a test nucleus: the error in the volume measurements was 0·39% and the error in the distance of the gravity centre from nucleus border was 1·52%. Thus we conclude that the error in the measurements caused by this additional noise could be considered as negligible.

Since we approximated the shape of the nucleus by its convex hull, we had to measure the level of errors introduced by the volume estimation. Indeed, because nuclei are not perfectly convex, the volume computed from the convex hull approximation tends to overestimate the actual volume of the nucleus. In order to measure this error a set of control cells with no silver staining was used. Since no silver labelling was done on these nuclei their shape is still near convex. The volume of each cell nucleus was measured after a segmentation/labelling step by counting the number of 'nuclear' voxels. Then the convex hull was calculated on each nucleus and we derived the volume by summing the subvolumes of the Voronoï tetrahedra. We found a modest systematic overestimation of the volume by 7·8% ± 0·01. Thus, we can assume for our material that the approximation of a nucleus by its convex hull does not introduce a large significant error in volume comparisons.

Segmentation

The segmentation is a process used on both the *AG* volume and the *NU* volume. The choice of a simple grey level

Table 2. Processing times for feature extraction on an Iris RS 4000 (R4000 100/50 MHz processor, 100 Mips, 16 MFlops, 70 Spec 89) with 64 MBytes of RAM. These times are workstation user times. Because potential users may be interested in the actual time of the feature extraction, we add the mean actual time of the process, taking into account the user's answers to the dialogue boxes.

Time spent for the *AG* volume processing		60 × 128 × 128 voxels
Median filtering	5 s	
Deblurring	1 min 10 s	
Binarization	1 s	
Labelling	2 s	14 objects labelled
Extraction of gravity centre	1 s	
Time spent for the *NU* volume processing		60 × 128 × 128 voxels
Median filtering	5 s	
Labelling	17 s	
Object extraction	2 s	
Surface extraction	1 s	16 000 surface points
Voronoï and convex hull	40 s	
Computation of parameters	1 s	
Effective time of the analysis of the two volumes	>1 min 26 s	The user had to select the operation in a menu bar and had to answer to dialogue boxes

threshold interactively set could be discussed. This technique remains subjective and could sometimes be irreproducible. The grey-level thresholding method presents two dependent biases: (i) the number of candidate threshold values is over a large range of grey-level values (≈10 in our case), (ii) the selection of these values is user-dependent.

In order to reduce this range, the grey-level values representing the frontier between object and background have to be reduced. Therefore, the image contrast is enhanced using the deblurring procedure in the case of the AgNOR images and using the confocal filter in the case of the nuclear images. Even after contrast enhancement, the segmentation procedure remains user-dependent. In order to reduce the effect of a subjective choice (i) only one user makes this choice for the entire analysis, (ii) the acquisition setting (contrast, brightness, scanning time, etc.) remained constant during the acquisition of all the cells, and (iii) the user assesses the result of their choice on orthogonal sections in the specimen.

Other methods, such as Voronoï tessellation (Bertin, 1993) or automatic threshold determination (Roysam, 1994), can be used to obtain more reproducible results. However, they are still too time-consuming to be used in the context of the analysis of a large number of specimens.

Processing time

The complete processing of a nucleus, including the acquisition step, took about 12 min. In practice, the analysis session was divided into two steps: (i) acquisition, transfer and storage of the data, and (ii) feature extraction. The time spent for each step of the analysis is shown in Table 2.

Conclusion

Until now, the existing methods developed to measure the distribution of AgNOR proteins were performed only in 2-D space. Today, the progress in microscopy and in computer sciences makes it possible to image biological specimens in three dimensions. In our approach, the use of a scanning laser microscope and a deblurring method allows us to develop an analysis based on 3-D information. Although the time spent for the analysis is increased by the amount of data that represent a 3-D description, the segmentation of AgNOR is facilitated by the deblurring technique and the distribution description is augmented by taking consideration of the third dimension. A preliminary study of three lines of cells (33 cells each) showed that the characterization of the AgNOR distribution can be used to differentiate cells belonging to different cell lines. This method of analysis could be used to assess the descriptive potential of the spatial distribution of AgNOR proteins in tumour pathology.

Acknowledgments

The authors wish to thank Dr Mark Overmars for providing the graphical interface builder, Dr Victoria von Hagen for her advice in editing the manuscript, Dr Raphaël Marcelpoil for his help in the elaboration of the 2-D convex hull, Dr Catherine Humbert for her advice on the biological part of the manuscript, and Dr Pierre Champelovier for providing the leukaemic cell lines and for his expert assistance.

References

Agard, D.A., Hiraoka, Y. & Sedat, J.W. (1989) Three-dimensional microscopy: image processing for high resolution subcellular imaging. *SPIE*, **1161**, 24–30.

Anderson, T.W. & Stephens, M.A. (1972) Tests for randomness of directions against equatorial and bimodal alternatives. *Biometrika*, **59**, 613–621.

Beorchia, A., Heliot, L., Menager, M., Kaplan, H. & Ploton, D. (1993) Application of medium-voltage STEM for the 3-D study of organelles within very thick sections. *J. Microsc.* **170**, 247–258.

Bertin, E. (1994) *Diagramme de Voronoï 2D et 3D–Application en imagerie*. PhD thesis. Université Joseph Fourier. Grenoble, France.

Bertin, E., Parazza, F. & Chassery, J.-M. (1993) Segmentation and measurement based on 3D Voronoï: application to confocal microscopy. *Computerized Medical Imaging and Graphics*, **17**, 175–182.

Boywer, A. (1993) Computing Dirichlet tesselation. *Comput. Journal*, **24**, 162–166.

Carter, K.C., Bowman, D., Carrington, W., Forgaty, K., McNeil, J.A., Fay, F.S. & Lawrence, J.B. (1993) A three-dimensional view of precursor messenger RNA metabolism within the mammalian nucleus. *Science*, **259**, 1330–1335.

Castleman, K.R. (1979) Three-dimensional image processing. *Digital Image Processing* (ed. by A.V. Oppenheim), pp. 351–360. Prentice Hall, Englewood Cliffs, NJ.

Conchello, J.-A. & Hansen, E.W. (1990) Enhanced 3-D reconstruction from confocal scanning microscope images 1: deterministic and maximum likelihood reconstructions. *Appl. Optics*, **29**, 3795–3804.

Crocker, J. & Skilbeck, N. (1987) Nucleolar organiser region associated proteins in cutaneous melanocytic lesions: a quantitative study. *J. Clin. Pathol.* **40**, 885–889.

Day, M. (1991) Parallel implementation of 3D convex-hull algorithm. *Computer Aided Design*, **23**, 177–188.

Derenzini, M., Nardi, F., Farabegoli, F., Ottinetti, A., Roncaroli, F. & Bussolati, G. (1989) Distribution of silver-stained interphase nucleolar organizer regions as a parameter to distinguish neoplastic reactive cells in human effusions. *Acta. Cytol.* **33**, 491–498.

Derenzini, M. & Ploton, D. (1991) Interphase nucleolar organizer regions in cancer cells. *Int. Rev. Exp. Pathol.* **32**, 149–192.

Egan, M.J. & Crocker, J. (1992) Nucleolar organiser regions in pathology. *Br. J. Cancer*, **65**, 1–7.

Gallagher, R., Collins, S., Trujillo, J., McCredie, K., Ahearn, M., Tsai, S., Metzgar, R., Aulakh, G., Ting, R., Ruscetti, F. & Gallo, R. (1979) Characterization of the continuous differentiating myeloid cell line (HL-60) from patient with acute promyelocytic leukemia. *Blood*, **54**, 713–733.

Gordon, D. & Reynolds, A. (1985) Image space shading of 3-dimensional objects. *Comp. Vision Graphics and Image Processing*, **29**, 361–376.

Guillaud, P., Wozniak, Z. & Seigneurin, D. (1993) Simultaneous quantitation of DNA and nucleolar organizer regions by image cytometry. *Analytical Quantitative Cyto. Histol.* **15**, 351–357.

Hernandez-Verdun, D., Robert-Nicoud, M., Geraud, G. & Masson, C. (1991) Behaviour of nucleolar proteins in nuclei lacking ribosomal genes. A study by confocal laser scanning microscopy. *J. Cell Sci.* **98**, 99–105.

Howell, W.M. (1982) *The Cell Nucleus* (ed. by H. Bush and L. Rothblum), Vol IX, pp. 89–142. Academic Press, New York.

Howell, W.M. & Black, D.A. (1980) Controlled silver staining of nucleolar organizer regions with a protective colloidal developer: one step method. *Experientia*, **36**, 1014–1023.

Kett, P., Geiger, B., Ehemann, V. & Komitowski, D. (1992) Three-dimensional analysis of cell nucleus structures visualized by confocal scanning laser microscopy. *J. Microsc.* **167**, 169–179.

König, D., Blackett, N., Clem, C.J., Downs, A.M. & Rigaut, J.-P. (1989) Orientation distribution of particle aggregates in 3D space based on point processes and laser scanning confocal microscopy. *Acta Stereol.* **8**, 213–218.

König, D., Carvajal-Gonzalez, S., Downs, A.M., Vassy, J. & Rigaut, J.-P. (1991) Modelling and analysis of 3-D arrangements of particles by point processes with examples of application to biological data obtained by confocal scanning light microscopy. *J. Microsc.* **161**, 405–433.

Lozzio, B.C. & Lozzio, B.B. (1975) Human chronic myelogenous leukemia cell-line with positive philadelphia chromosome. *Blood*, **45**, 321–334.

Mattfeldt, T., Clarke, A. & Archenhold, G. (1994) Estimation of the directional distribution of spatial fibre processes using stereology and confocal laser microscopy. *J. Microsc.* **173**, 87–101.

Parazza, F., Humbert, C. & Usson, Y. (1993). Method for 3D volumetric analysis of intranuclear fluorescence distribution in confocal microscopy. *Computerized Medical Imaging and Graphics*, **17**, 189–200.

Ploton, D., Bobichon, H. & Adnet, J.J. (1982) Ultrastructural localization of NOR in nucleoli if human breast cancer tissues using a one-step AgNOR staining method. *Biol. Cell*, **43**, 229–232.

Ploton, D., Menager, M., Jeannesson, P., Himber, G., Pigeon, F. & Adnet, J.J. (1986) Improvement in the staining visualization of the argyrophilic proteins of the nucleolar organiser regions at the optical level. *Histochem. J.* **18**, 5–14.

Preparata, F.P. & Shamos, M.I. (1985) *Computational Geometry. An Introduction* (ed. by D. Gries), pp. 198–214. Springer-Verlag, New York.

Preston, K. Jr. & Siderits, R. (1992) New techniques for three-dimensional data anlysis in histopathology. *Analytical Quantitative Cytol. Histol.* **14**, 398–406.

Reif, J.H. & Sen, S. (1992) Optimal parallel randomized algorithms for three-dimensional convex hulls and related problems. *SIAM J. Comput.* **21**, 466–485.

Robb, R.A. & Barillot, C. (1988) Interactive 3-D image display and analysis. *SPIE*, **939**, 173–202.

Robert-Fortel, I., Junéra, H.R., Géraud, G. & Hernandez-Verdun, D. (1993) Three-dimensional organization of ribosomal genes and AgNOR proteins during interphase and mitosis in PtK1 cells studied by confocal microscopy. *Chromosoma*, **102**, 146–157.

Roysam, B., Ancin, H., Battacharjya, A.K., Chisti, M.A., Seegal, R. & Turner, J.N. (1994) Algorithms for automated characterization of cell populations in thick specimens form 3-D confocal fluorescence microscopy data. *J. Microsc.* **173**, 115–126.

Rüschoff, J., Plate, K.H., Contractor, H., Kern, S., Zimmerman, R. & Thomas, C. (1990) Evaluation of nucleolus organizer regions (NORs) by automatic image analysis: a contribution to standardization. *J. Pathol.* **161**, 113–118.

Seigneurin, D., Champelovier, P., Mouchiroud, G., Berthier, R., Leroux, D., Prenant, M., McGregor, J., Starck, J., Morle, F., Micouin, C., Pietrantuono, A. & Kolodie, L. (1987) Human chronic myeloid leukemic cell line with positive Philadelphia chromosome exhibits megakaryocytic and erythroid characteristics. *Exp. Hematol.* **15**, 822–832.

Shaw, P.J. & Rawlins, D.J. (1991) Three-dimensional fluorescence microscopy. *Prog. Biophys. Molec. Biol.* **56**, 187–213.

Usson, Y., Parazza, F., Jouk, P.-S. & Michalowicz, G. (1994) Method for the study of the three-dimensional orientation of the nuclei of myocardial cells in fetal human heart by means of confocal scanning laser microscopy. *J. Microsc.* **174**, 101–110.

van der Voort, H.T.M., Brakenhoff, G.J. & Baarslag, M.W. (1989) Three-dimensional visualization methods for confocal microscopy. *J. Microsc.* **153**, 123–132.

Wachtler, F., Hopman, A.H.N., Wiegant, J. & Schwarzacher, H.G. (1986) On the position of nucleolus organizer regions (NORs) in interphase nuclei. *Exp. Cell Res.* **167**, 227–240.

Willis, B., Roysam, B., Turner, J.N. & Holmes, T.J. (1993) Iterative, constrained 3-D image reconstruction of transmitted light bright-field micrographs based on maximum likelihood estimation. *J. Microsc.* **169**, 347–361.

Appendix

Three-dimensional distance of a gravity centre of an AgNOR aggregate from a triangle of the convex hull triangulation

1 The coordinates $(x_{g'}, y_{g'}, z_{g'})$ of a point g' belonging to the plane P defined by the three vertices, $a(x_a, y_a, z_a)$, $b(x_b, y_b, z_b)$, $c(x_c, y_c, z_c)$, of a triangle of the convex hull triangulation are given by

$$\begin{aligned} x_{g'} &= K_2 \times x_v + K_3 \times x_u + x_a \\ y_{g'} &= K_2 \times y_v + K_3 \times y_u + y_a \\ z_{g'} &= K_2 \times z_v + K_3 \times z_u + z_a \end{aligned} \tag{1}$$

where

$$\vec{V} = \begin{pmatrix} x_v \\ y_v \\ z_v \end{pmatrix} = \begin{pmatrix} x_b - x_a \\ y_b - y_a \\ z_b - z_a \end{pmatrix}, \quad \vec{U} = \begin{pmatrix} x_u \\ y_u \\ z_u \end{pmatrix} = \begin{pmatrix} x_c - x_a \\ y_c - y_a \\ z_c - z_a \end{pmatrix},$$

and $K_2 K_3$ are real coefficients.

2 The coordinates of a point g' belonging to the line going through an AgNOR aggregate gravity centre g with the direction $\vec{N}$ (normal to P) are given by

$$\begin{aligned} x_{g'} &= K_1 \times x_N + x_g \\ y_{g'} &= K_1 \times y_N + y_g \\ z_{g'} &= K_1 \times z_N + z_g \end{aligned} \tag{2}$$

where the coordinates of the normal vector $\vec{N}$ are given by the cross product $\vec{V} \wedge \vec{U}$ and K_1 is a real coefficient.

3 The coordinates of the point g' resulting to the orthogonal projection of the point g on the plane P are obtained by finding the coefficient K_1 of the linear system of equations

$$\begin{aligned} x_g - x_a &= -K_1 \times x_N + K_2 \times x_v + K_3 \times x_u \\ y_g - y_a &= -K_1 \times y_N + K_2 \times y_v + K_3 \times y_u \\ z_g - z_a &= -K_1 \times z_N + K_2 \times z_v + K_3 \times z_u \end{aligned} \tag{3}$$

$$K_1 = \frac{1}{\begin{vmatrix} -x_N & x_v & x_u \\ -y_N & y_v & y_u \\ -z_N & z_v & z_u \end{vmatrix}} \times \begin{vmatrix} x_g - x_a & x_v & x_u \\ y_g - y_a & y_v & y_u \\ z_g - z_a & z_v & z_u \end{vmatrix}. \tag{4}$$

Using the value of K_1 in Eq. (2), the coordinates of g' can be found. Then it becomes possible to calculate the distance (g', g) (distance of the gravity centre of an AgNOR aggregate from a triangle of the convex hull).